small structures
www.small-structures.com

Seeded-Growth of PCN-224 onto Plasmonic Nanoparticles: Photoactive Microporous Nanocarriers

Manuel Ceballos, Samuel Funes-Hernando, Giulia Zampini, Manuela Cedrún-Morales, José Manuel Vila-Fungueiriño, Beatriz Pelaz, and Pablo del Pino**

This study addresses the fabrication of microporous plasmonic nanocomposites (NCs) by using plasmonic nanoparticles (i.e., gold bipyramids, AuB) as seeds to grow microporous shells, specifically, metal–organic frameworks (MOF) PCN-224 of increasing thickness from 69 to 138 nm. This method is based on using a previously synthesized Zr_6-oxo cluster and unfolds at room temperature. Notably, it is demonstrated that the concentration of the AuB seeds determines both the yield of NCs and the resultant thickness of the PCN-224 shell, illustrating the seeded growth mechanism. Furthermore, it is found that the thermoplasmonic response of the NCs is dominated by the thickness of the microporous shell, with thicker shells having enhanced thermal confinement properties than thinner ones. As a proof of concept, the NCs are loaded with cresyl violet (CV), a lysosomal fluorescent marker. This serves to demonstrate the thermoplasmonic-induced intracellular release of CV by the photostimulation of the AuB's plasmonic near-infrared (NIR) band. Moreover, the NCs display exceptional efficacy as photodynamic agents when photostimulated at the PCN-224's Soret band. In summary, this study offers a facile, efficient, and reproducible methodology for the fabrication of NCs with a controlled geometry while unlocking new possibilities in the field of nanoMOFs as multifunctional theranostic probes.

1. Introduction

Metal–organic frameworks (MOFs) represent an emergent category of solid, porous, and crystalline materials characterized by the coordination of metal ions or inorganic secondary building units (SBUs) with an extensive network of organic linkers.[1–3] These linkers primarily encompass carboxylates, like UiOs family,[4] phosphates,[5] imidazole rings, like in ZIFs family,[6] and nonconventional functional groups like hydroxamate,[7] among others. MOFs have garnered significant attention owing to their exceptional physicochemical attributes, including high surface area,[8–11] customizable porosity,[12] amenable postsynthetic modification,[13] and precise control over particle size,[14,15] among others. These properties render MOFs suitable for applications spanning diverse domains. Notably, MOFs find utility in the field of biotechnology, in many bioapplications[16–18] serving as carriers and platforms for drug delivery systems (DDSs).[19,20] In the energy sector, MOFs exhibit promise as gas storage materials[21] and as electrode materials for advanced batteries.[22] Additionally, MOFs hold relevance in water resource management with applications in water harvesting,[23] and they contribute significantly to environmental remediation systems[24] and photocatalytic materials for sustainable solutions.[25]

Zirconium-based metal–organic frameworks (Zr-MOFs) have gained substantial attention, since the advent of UiO-66,[4] owing to their exceptional attributes such as remarkable thermal, chemical, and structural stability. Additionally, the presence in these frameworks of the $Zr_6O_4(OH)_4$ as SBU, which can accommodate up to twelve carboxylate linkers,[26] presents a unique opportunity

M. Ceballos, S. Funes-Hernando, M. Cedrún-Morales, P. del Pino
Centro Singular de Investigación en Química Biolóxica e Materiais Moleculares (CiQUS)
Departamento de Física de Partículas
Universidade de Santiago de Compostela
15782 Santiago de Compostela, Spain
E-mail: pablo.delpino@usc.es

The ORCID identification number(s) for the author(s) of this article can be found under https://doi.org/10.1002/sstr.202300464.

DOI: 10.1002/sstr.202300464

G. Zampini
Centro Singular de Investigación en Química Biolóxica e Materiais Moleculares (CiQUS)
Universidade de Santiago de Compostela
15782 Santiago de Compostela, Spain

J. M. Vila-Fungueiriño
Centro Singular de Investigación en Química Biolóxica e Materiais Moleculares (CiQUS)
Departamento de Química Física
Universidade de Santiago de Compostela
15782 Santiago de Compostela, Spain

B. Pelaz
Centro Singular de Investigación en Química Biolóxica e Materiais Moleculares (CiQUS)
Departamento de Química Inorgánica
Universidade de Santiago de Compostela
15782 Santiago de Compostela, Spain
E-mail: beatriz.pelaz@usc.es

to diversify the landscape of MOF materials. This property affords the prospect of generating an extensive array of MOFs characterized by distinct chemical compositions, crystal structures, and topologies. The class of zirconium-based porphyrinic metal–organic frameworks (Zr-porphyrinic MOFs) serves as a noteworthy exemplar of this phenomenon. Changes in the structural connectivity of the SBU in these porphyrinic frameworks instigate crystallographic variations, manifesting in six distinct polymorphs.[27] These polymorphs are possible due to the utilization of the $Zr_6O_4(OH)_4$ SBU in conjunction with the tetratopic porphyrinic linker, tetrakis(4-carboxyphenyl)porphyrin (TCPP), exhibiting diverse connectivities. These include the 12-connected (12-c) MOFs, MOF-525[28] and PCN-223,[29] the 8-connected MOFs, MOF-545/PCN-222,[28,30] PCN-225,[31] and NU-902,[32] as well as the 6-connected (6-c) MOF, PCN-224.[33] These MOFs collectively exhibit intriguing optoelectronic properties, and high chemical and structural long-term stability,[33–37] rendering them highly pertinent in applications spanning biotechnology, catalysis, and energy conversion systems.[38]

In contrast, plasmonic nanoparticles (NPs) represent a distinct class of inorganic nanomaterials characterized by their remarkable optical properties, attributed to the collective oscillation of conduction electrons on their surfaces, known as localized surface plasmon resonance (LSPR).[39,40] Many of the LSPR frequencies match within the visible electromagnetic spectrum. However, it is possible to tailor and manipulate LSPR to occur within the near-infrared (NIR) region by modulating various factors, including the choice of capping agents, the dielectric environment, particle size, material, and most significantly, particle morphology.[41] In contrast to isotropic particles that according to Mie's theory can generate just a single LSPR mode,[42] anisotropic NPs, such as rods,[43] triangles,[44] cubes,[45] stars,[46] or bipyramids,[47] generate multiple LSPR modes by the ability of their electron clouds to oscillate in diverse directions. Plasmonic NPs find wide-ranging utility in diverse applications, including but not limited to substance sensing, surface-enhanced Raman spectroscopy,[48] antifungal agents,[49] and photothermal therapy.[50] This versatility arises from the capacity of these NPs to generate localized heat through the excitation of their LSPR. This is particularly valuable in bioapplications,[51] especially when photoactivated within the biological window, including photocontrolled drug delivery,[52–54] photothermal therapy,[55] optoacoustic imaging,[56] and plasmonic-driven thermal biosensing.[57]

Combining the characteristics of metal–organic frameworks at the nanoscale (NMOFs) and plasmonic NPs has led to a novel class of nanocomposites (NCs) characterized by exceptional properties.[58] Unfortunately, the development of core@shell systems, such as incorporating plasmonic NPs within MOFs (NPs@NMOF), poses considerable challenges. This difficulty primarily arises from the rigorous synthetic conditions typically associated with MOF production, involving elevated temperatures (>100 °C), extended reaction times (typically 24 h), and the use of organic solvents, most commonly dimethylformamide (DMF). These conditions are often incompatible with the stability of plasmonic NPs or others.

The advancement of core@shell systems, wherein inorganic NPs are employed as the core while NMOFs serve as the outer shell, has recently been established as an exciting new research area. For example, when the core is a plasmonic NP, these systems present the remarkable storage capabilities of NMOFs, capable of encapsulating a wide range of molecules, including drugs and dyes, in tandem with the potent heating capabilities of plasmonic NPs. This synergy has paved the way for the development of remotely-controlled nanomaterials capable of selectively releasing cargo through the thermodiffusion process, commonly referred to as the Soret effect.[59] For instance, MOFs like ZIF-8 can be effectively grown using plasmonic NPs as seeds, such as Au nanostars, creating versatile NCs that can be remotely activated for cargo release,[52] or thermal reactions,[53] even inside living cells. Additionally, catalytic NPs, like palladium, can be incorporated to facilitate uncaging reactions also in living cells.[60] The growth mechanism of these MOFs is well-established with MOF crystallinity correlated to the quantity of surfactant present on the NP´s surface.[61] However, a notable drawback of ZIF-8 is its limited chemical and structural stability in aqueous environments, primarily due to the formation of $ZnCO_3$ resulting from the interaction with dissolved CO_2 in water.[62] To solve this issue, it is necessary to further functionalize these NCs, for example, using amphiphilic polymers, which inhibit degradation and enhance their stability in aqueous media.[52,53,60]

Here, we present a simple, fast, and efficient synthesis of core@shell NCs that occur at mild conditions, i.e., room temperature (RT) and short reaction time (1 h). These NCs comprise a gold bipyramid (AuB) NP as core and PCN-224 Zr-porphyrinic NMOF as shell (Figure S1, Supporting Information). AuB is functionalized with thiol-polyethylene glycol (HS-PEG), which provides them with stability in DMF. The PCN-224 shell has been loaded with cresyl violet (CV), as model cargo, to demonstrate its light-triggered induced-release under NIR laser irradiation within living cells and prove the photodynamic properties of the MOF (**Scheme 1**).

2. Results and Discussion

2.1. Synthesis and Structural Characterization of PCN-224 NMOFs and NCs

The use of a preformed Zr_6-oxo cluster has been described in some syntheses of Zr-based MOFs such as PCN-222[63] and NU-901.[64] This synthetic approach offers the benefit of preventing the formation of secondary phases or mixed phases. In this study, PCN-224 in its pure phase (Figure S1, Supporting Information), without the presence of other polymorphs, was synthesized using the mentioned cluster with acetic acid as modulator. The preformed cluster was characterized by thermogravimetric analysis (TGA) and powder X-ray diffraction (PXRD). The synthesis of the cluster was conducted in 1-propanol, followed by washing with the same solvent to remove any excess of benzoic acid. Subsequently, the sample was dried under a vacuum. TGA results confirmed the presence of 1-propanol even after dry-freezing. Therefore, an additional washing step with methanol (MeOH), followed by vacuum drying was required (Figure S2a, Supporting Information). Approximately 50% of the initial amount of 1-propanol used in the synthesis, remained after drying in a vacuum for a day. The cluster exhibited a good crystallinity after the removal of 1-propanol washing it with MeOH and drying in vacuum (Figure S2b, Supporting Information). The

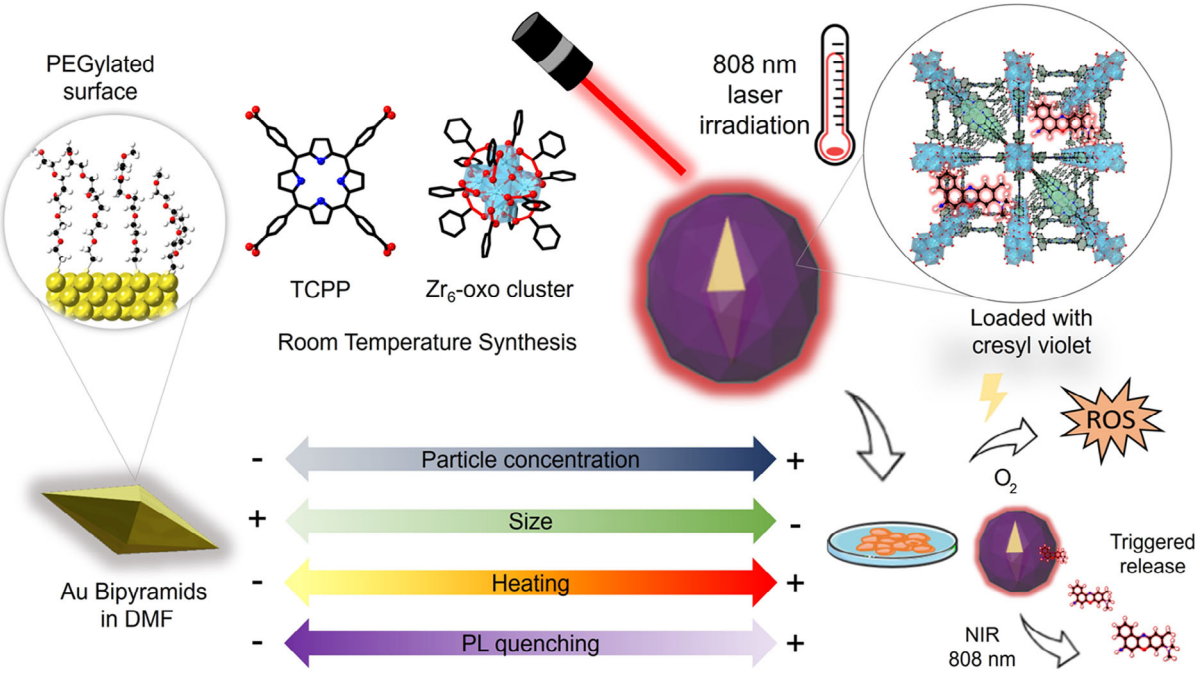

Scheme 1. Scheme of work representing the use of PEGylated AuB as core with PCN-224 as shell loaded with CV. CV is released under NIR light while the PCN-224 linker is capable of both generating a fluorescence signal and producing ROS upon visible irradiation. Also, it is depicted as a summary of the effect of AuB concentration in size, heating, and luminescent properties of the AuB@PCN-224 NCs.

cluster was analyzed by inductively coupled plasma (ICP), which yielded a Zr content of 22.67%, in good agreement with the 22.18% obtained via TGA. These values closely align with the theoretically expected Zr content of 25.66% (Figure S2c, Supporting Information), taking into consideration the coordination of twelve benzoate molecules to the cluster.

The synthesis of PCN-224 at RT was conducted using two types of clusters: 1) the nonwashed cluster containing 1-propanol (PCN-224-p) in which the ratio linker (TCPP)/metal (Zr) was 1.3 while the ratio modulator (HOAc)/metal (Zr) was 1450; and 2) the washed cluster that was thoroughly cleaned with MeOH to remove completely the 1-propanol (PCN-224-w) in which the ratios were TCPP/Zr 0.25 and HOAc/Zr 290 (Table S1, Supporting Information). **Figure 1**a–c shows field-emission scanning electron microscopy (FE-SEM) images of PCN-224 NCs with AuB core (Figure S3, Supporting Information). The particles obtained in each case showed distinct sizes and polydispersity degrees. Figure S4, Supporting Information, shows a FE-SEM image of PCN-224-p, PCN-224-w here is possible to appreciate the difference in polydispersity using their cluster with 1-propanol or the washed cluster PCN-224-p rendered highly polydisperse particles ranging from 150 to 900 nm, whereas PCN-224-w produced highly monodisperse NMOFs of about 150 nm (Figure S4 and Table S2, Supporting Information). Figure 1d–e shows transmission electron microscopy (TEM) and high-resolution (HR)-TEM images of PCN-224-w corroborating the monodispersity and crystallinity of the NMOFs. The reaction time, temperature, and modulator amount were kept identical for both experiments. However, the ratio of linker to modulator differs due to the presence or absence of 1-propanol in the cluster. Compared with the highly monodisperse sample PCN-224-w, the polydispersity of PCN-224-p can be attributed to both the presence of 1-propanol and the difference in the linker-modulator ratio. Interestingly, when the synthesis of MOF using the cluster PCN-224-p was carried out with the presence of PEGylated AuB (83 nm length per 28 nm width, Figure S3, Supporting Information), we obtained extraordinarily monodisperse core@shell NCs (Figure 1f–g and S4, Supporting Information). Moreover, NCs using PEGylated Pd nanocubes (PdNPs) instead of AuB were also equivalently produced, proving that our method is suitable for other inorganic NPs (Figure S5, Supporting Information).

Results confirmed that the presence of 1-propanol appears crucial to obtain these NCs, as we were unable to obtain core@-shell nanosystems using the 1-propanol-free cluster used for PCN-224-w (Figure S6, Supporting Information). We hypothesize that 1 propanol likely acts as a cosurfactant in the presence of AuB and interacts with the PEG chains promoting an enhanced local accumulation of Zr_6-oxo clusters in the oxygen moieties of the PEG monomers. Energy-dispersive X-ray spectroscopy–scanning transmission electron microscopy (EDX–STEM) analysis of AuB(10)@PCN-224 (Figure 1h–l) corroborated the presence and distribution of C and O due to the linker (TCPP), Zr due to the Zr_6-oxo cluster, and Au in the core for the bipyramids.

Figure 1c,d illustrates the AuB@PCN-224 NCs obtained by introducing increasing amounts of PEGylated AuB (1, 5, and 10 nM) in the reaction mixture, while keeping precisely the same reaction conditions as to produce PCN-224-p. Using a concentration of 1 nM, the NCs exhibit a thicker MOF shell (AuB(1)@PCN-224), and as the concentration increases (AuB(5)@PCN-224 and

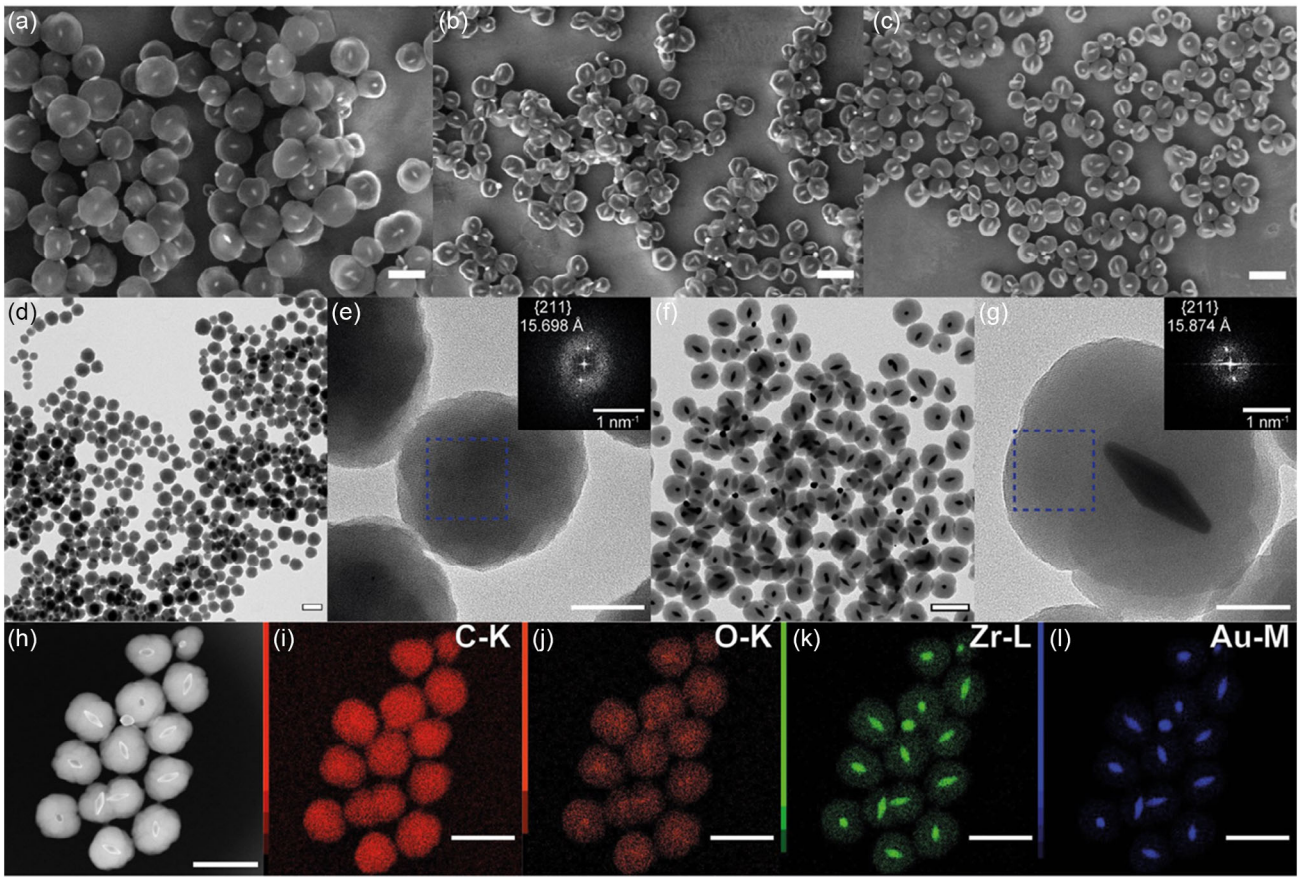

Figure 1. FE-SEM images of a) AuB(1)@PCN-224, b) AuB(5)@PCN-224, and c) AuB(10)@PCN-224. d) TEM image and e) HR-TEM image with FFT of PCN-224-w. f) TEM image and g) HR-TEM image with FFT of AuB(10)@PCN-224. h–l) EDX–STEM analysis of AuB(10)@PCN-224. Scale bars 250 nm except HR-TEM images (e,g) are 50 nm.

AuB(10)@PCN-224), the thickness of the shell decreases progressively with very good reproducibility among batches (Figure S7, Supporting Information). We also observed that the presence of seeds increased the yield (Zr) of the reaction as determined by ICP with respect to both PCN-224 systems (Figure S8, Supporting Information). Figure 1h presents a TEM image of AuB(10)@PCN-224, revealing a distinctive core-shell structure where a single AuB is encapsulated within the center of the MOF shell.

Figure 1e,g displays HR-TEM images accompanied by a fast Fourier transform (FFT) analysis of PCN-224-w and AuB(10)@PCN-224, respectively. The FFT measurement reveals a d-spacing value of 15.689 Å for PCN-224-w and 15.874 Å for AuB(10)@PCN-224, which corresponds to the {211} family of crystallographic planes. In a cubic system with a lattice parameter of 38.4520 Å and space group $Im\bar{3}m$, the expected *d*-spacing for the {211} planes is 15.698 Å.[33]

Figure 2a presents the UV–vis absorption spectra of the prepared samples. In the case of PCN-224-p (pink line), a considerably broad Soret band is observed, with a maximum absorbance at around 420 nm, owing to the polydispersity in this sample. Additionally, four *Q* bands exhibit scattering, which can be attributed to the presence of larger particles (>1 μm). Conversely, PCN-224-w (black line) displays a distinct and narrow Soret band, accompanied by the absence of scattering in the *Q* bands, in agreement with a smaller particle size. The large difference in polydispersity between the PCN-224-p and PCN-224-w was also confirmed by dynamic light scattering (DLS) analysis (Figure 2b). Moreover, in the UV–vis spectra of the NCs (AuB@PCN-224) analogous absorption bands to PCN-224-w were identified, while the characteristic longitudinal LSPR centered at 810 nm from the AuB was also present. The plasmonic-to-Soret peak ratios increased as more seeds were used. These spectra agree with the formation of core@shell NCs. Furthermore, a slight blue shift in the LSPR peak is observed in Figure 2a, which can be attributed to the influence of the PCN-224 shell thickness on the surrounding dielectric environment. DLS analysis showed monodispersed colloidally stable samples (Figure 2b). Increasing AuB concentrations led to smaller hydrodynamic diameters, in line with the formation of NCs with thinner PCN-224 shells. Figure 2c shows Fourier transform infrared (FT-IR) spectra of the systems, showing the characteristic C═O vibration in TCPP linker at 1690 cm^{-1}, which is absent in PCN-224 samples due to the formation of coordination bond between Zr—O and the vibration of O—C—O ant 1609 and 1417 cm^{-1}.

The crystalline nature of all the particles was confirmed by PXRD analysis (Figure 2d). The obtained diffraction patterns

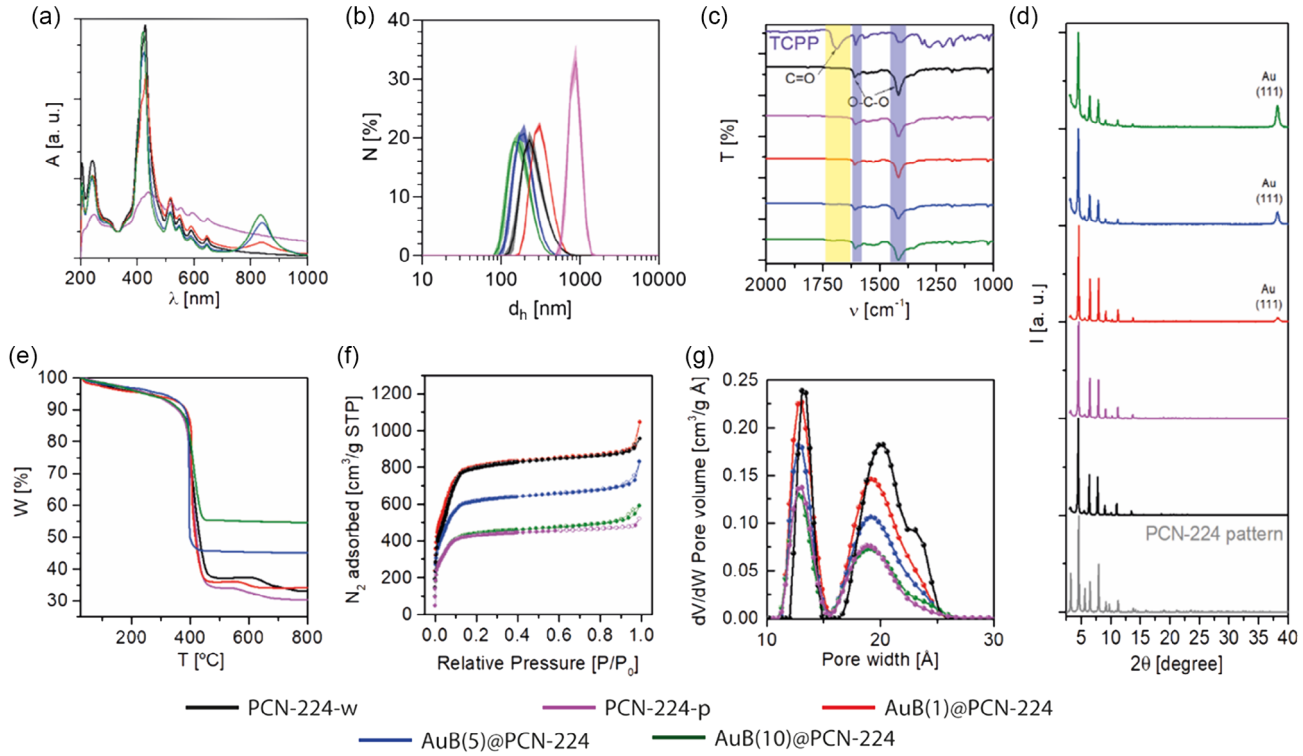

Figure 2. Characterization of PCN-224 NPs and the NCs: a) UV–vis spectra, b) DLS particle size distribution, c) FT-IR analysis, d) PXRD diffractogram, e) TGA analysis, f) N_2 adsorption isotherms, and g) porous size distribution.

indicated the presence of the pure-phase PCN-224. The main diffraction peaks were observed at 3.204°, 4.616°, 5.553°, 6.433°, 7.893°, and 9.113° two-theta degree, corresponding to the crystallographic planes (110), (200), (211), (220), (222), and (400), respectively. These findings indicate that the crystallinity of the PCN-224 material was unaffected by the presence of 1-propanol or AuB during the synthesis. Notably, the presence of Au was observed in the corresponding NCs. The diffraction pattern exhibited a peak at 38.200° two-theta degree, corresponding to the Au (111) crystallographic plane.

TGA reveals the stability of the samples up to a temperature of 400 °C (Figure 2e). Comparative analysis between PCN-224-p and PCN-224-w shows that PCN-224-p exhibited a lower presence of inorganic residue (ZrO_2) than PCN-224-w. This disparity can be attributed to the existence of missing linker defects in PCN-224-w caused by a low linker/metal (L/M) ratio. Specifically, PCN-224-p possessed a L/M ratio of 1.45, while PCN-224-w had a L/M ratio of 0.30. Additionally, an increase in the concentration of AuB resulted in a gradual increase in the quantity of inorganic residue. The estimation of the gold amount (Au) was performed by subtracting the plateau value of PCN-224-w from the plateau value of samples with gold (**Table 1**).

The porosity of PCN-224 samples was assessed through N_2 adsorption measurements conducted at 77 K (Figure 2f). The N_2 uptake for PCN-224-w was determined to be 910 $cm^3\,g^{-1}$ at standard temperature and pressure (STP), accompanied by a brunauer-emmett-teller (BET) surface area of 2624 $m^2\,g^{-1}$. In comparison, PCN-224-p exhibited a N_2 uptake of 480 $cm^3\,g^{-1}$ (STP) and a BET surface area of 1377 $m^2\,g^{-1}$. These findings indicate that PCN-224-w possesses superior crystallinity when compared to PCN-224-p, which can be corroborated by a decrease in the pore volume in the porous size distribution (Figure 2g). The N_2 uptake of the composites exhibited a gradual decrease while increasing the gold content. This decrease can be attributed to the presence of nonporous Au mass, which reduces the available porous space for N_2 adsorption. Furthermore, the BET surface areas were corrected by subtracting the percentage of Au obtained through TGA analysis (Figure 2e). Interestingly, the sample with the lower amount of Au (1 wt%, AuB(1)@PCN-224) showed nearly the same BET surface area as PCN-224-w, indicating minimal impact on porosity. However, as the amount of Au increased decreasing the thickness of the shell, the BET surface areas decreased. We speculatively correlate this reduction to the presence of PEG molecules which can fill the pores in the

Table 1. BET surface area and percentage of Au in PCN-224 and NCs.

Sample	BET surface area [$cm^3\,g^{-1}$]	% Au	Corrected BET surface area [$cm^3\,g^{-1}$]
PCN-224-w	2647.22 ± 45.09	–	–
PCN-224-p	1377.14 ± 19.53	–	–
AuB(1)@PCN-224	2598.43 ± 39.79	1.00	2624.68 ± 40.19
AuB(5)@PCN-224	1988.85 ± 29.41	12.02	2260.57 ± 33.43
AuB(10)@PCN-224	1425.09 ± 20.33	21.26	1809.87 ± 25.82

Au-PCN-224 interface (i.e., Au-S-PEG-PCN-224),[64] thereby increasingly affecting the accessible surface area for gas adsorption as the MOF thickness decreases (Table 1).

2.2. Effect of Shell Thickness in Photoluminescent Properties

Aiming to systematically evaluate the influence of varying MOF shell thickness on the optical properties of our systems, two additional NCs were prepared, AuB(2)@PCN-224 and AuB(3)@PCN-224, to complete a comprehensive library (**Figure 3**a–e for AuB 1, 2, 3, 5, and 10 nM, respectively). For these two new samples, the amount of starting PEGylated AuB during the synthesis process was fixed at 2 and 3 nM, respectively. The produced NCs present a highly homogeneous core@shell structure in which the AuB is centered at the NCs. Therefore, we can assume considering the geometric feature of the NCs that bipyramids are coated with a NMOF PCN-224 shell of ≈138, 112, 108, 80, and 69 nm, for AuB(1)@PCN-224, AuB(2)@PCN-224, AuB(3)@PCN-224; AuB(5)@PCN-224, and AuB(1)@PCN-224, respectively, as measured from the FE-SEM images.

To make easier the rationalization of the results (displayed in Figure 3f–g), the concentrations of the NCs were systematically adjusted to provide the same absorption value at the used excitation wavelength (420 or 515 nm, alternatively).

The emission profile of PCN-224-w closely resembles that of the porphyrinic precursor (TCPP), exhibiting two emission bands at 650 and 720 nm. The presence of AuB within the core of the particles NCs does not alter the emission profile (Figure 3f–g and S9, Supporting Information), which is also supported by the superimposable excitation spectra of PCN-224 (Figure S10, Supporting Information). However, it significantly affects the photoluminescence (PL) intensity of the samples. Notably, this effect is dependent on the excitation wavelength used. Excitation at 420 nm (Figure 3f), which lies outside the main absorption range of the AuB core (500–850 nm, Figure S3a, and S11, Supporting Information), leads to significant PL quenching in the NCs, albeit with slight variations among them. Conversely, when an excitation wavelength in resonance with the AuB plasmon is employed (515 nm, Figure 3g), a clear decreasing trend of PL intensity from AuB(1)@PCN-224 to AuB(10)@PCN-224 is observed (Table S3, Supporting Information).

The pathways affecting the PL of a system can be various, like intersystem transitions, energy transfer, and thermal radiation, among others. Among these mechanisms, Förster resonance energy transfer and nanosurface energy transfer are recognized as relevant theories explaining fluorescence quenching by gold nanomaterials.[65,66] However, due to the complexity of PCN-224 system, it is important to acknowledge that other energetic radiationless processes can be affected by the presence of gold nanomaterials, such as the intersystem crossing yield or the energy transfer to molecular oxygen to produce photoinduced reactive oxygen species (ROS).[67–69]

Nevertheless, to definitively attribute the observed PL quenching to the presence of AuB, time-resolved analysis was performed. Through time-correlated single photon counting technique, the PL decay kinetics of PCN-224 NMOFs and the relative NCs were acquired by exciting the samples at 375 nm (Figure 3h). Based on the data depicted in Figure 3h, it is unlikely to detect a

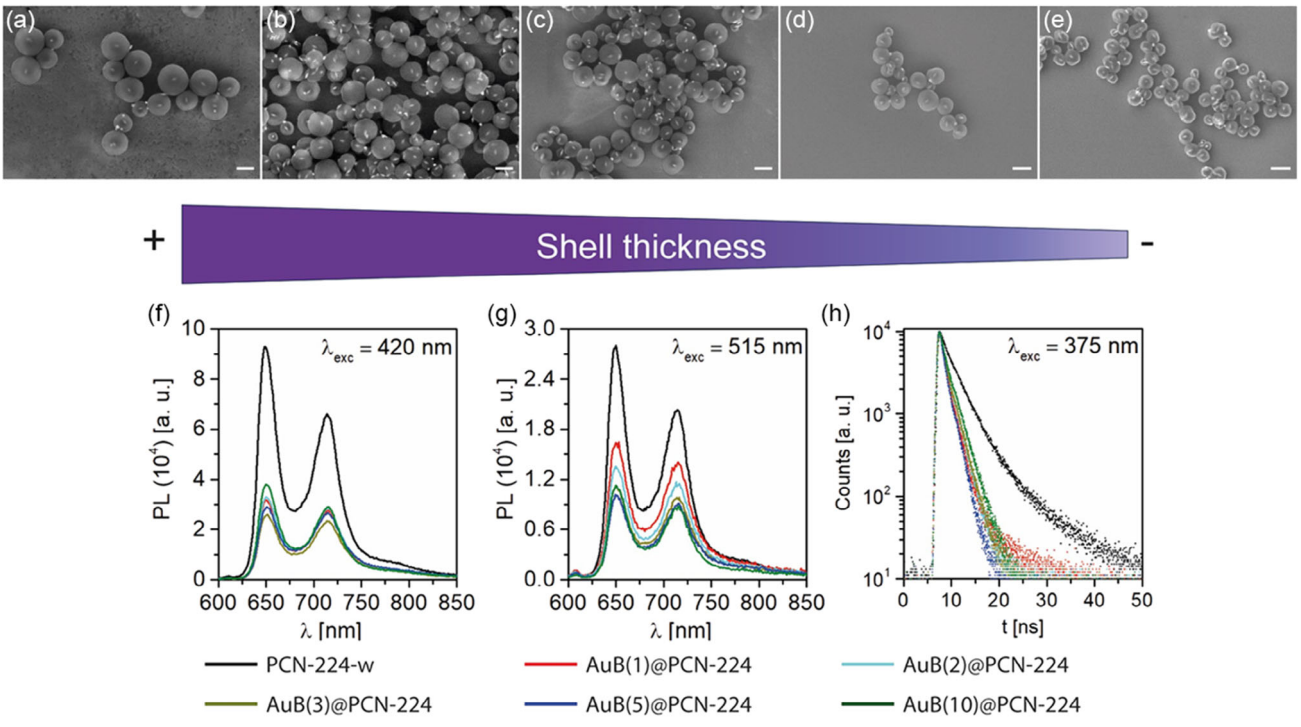

Figure 3. a–e) FE-SEM images of AuB@PCN-224 NCs using 1, 2, 3, 5, and 10 nM AuB concentration, respectively, showing a decrease in the cell thickness. Corrected PL emission spectra of PCN-224 NPs and the NCs by exciting the samples at f) 420 nm; g) 515 nm; and h) time-correlated single photon counting decay kinetics (excitation at 375 nm).

substantial disparity among the NCs by using this excitation wavelength. However, a distinct variation is clearly observed when compared to PCN-224 NMOFs.

The recorded decay times were analyzed using a multiexponential function (Equation S(1), Supporting Information), which indicates the existence of multiple luminescent components within our systems (Table S4, Supporting Information). The decay times of PCN-224 NMOFs align with the literature data.[70–72] However, with the introduction of AuB, a notable reduction in the decay times (τ) is observed, with the average decay time halved. Furthermore, when analyzing the luminescent components individually, additional observations can be made. The longer component of PCN-224 (6.9 ns) is in very good agreement with the value reported for PCN-224 in anoxic environment.[71] Considering that our measurements are conducted in an air-saturated condition, this longer component can be assigned to the porphyrin molecules located within the core of PCN-224 particles, which are shielded from external oxygen, resulting in their longer decay times. Nevertheless, the external porphyrin molecules and the ones within the porous channels undergo an effective quenching process, causing a reduction in the decay time to approximately 2.6 ns.

Considering the relative positions of AuB and the PCN-224 network, it can be reasonably assumed that the molecules in close proximity to the gold surface, thus within the core, experience a more pronounced quenching effect. In the case of AuB(1)@PCN-224, with a thicker PCN-224 shell, the PCN network directly coordinated to the gold surface undergoes substantial PL quenching, even if the higher shell thickness allows the longer component to still exist, albeit with a significant lower percentage (5%, Table S4, Supporting Information). Similar observations and conclusions can be drawn for the other NCs, despite the absence of a longer decay component, which is likely due to the thinner PCN shell in those cases.

These findings collectively illustrate the direct influence of AuB on the photophysical behavior of the PCN-224, playing a role in the PL processes; moreover, by manipulating the thickness of the PCN-224 shell (Table S2, Supporting Information), different outcomes can be achieved in terms of the observed photophysical behavior.

2.3. Heating Properties of AuB@PCN-224@PEG NCs under 808 nm Laser Irradiation

Prior to investigating the photothermal characteristics of the plasmonic AuB@PCN-224 NCs, the NCs were functionalized with mPEG-PO_3 (Figure S12, Supporting Information). This functionalization was verified with FT-IR, where characteristic stretching vibrations of $-CH_2-$ at 2869 cm^{-1}, –P–O at 1098 cm^{-1}, and a broadband corresponding to –O–H at 3433 cm^{-1} were observed (Figure S13, Supporting Information).[63] The purpose of this functionalization was to enhance the colloidal stability of the NCs to prevent NP aggregation, which could be caused by increased Brownian motion during heating. As an initial step, the samples were transferred from methanol (MeOH) to water, resulting in a blue shift in the LSPR due to the change in the dielectric environment (Figure S14a, Supporting Information). Furthermore, the hydrodynamic size of the NCs according to DLS and nanoparticle tracking analysis results, increased compared to the unmodified system (Figure S15 and Table S5, Supporting Information), and their ζ-potential shifted from positive to negative values, as expected (Figure S16, Supporting Information). This shift was attributed to the presence of Zr atoms on the surface that neutralize their positive charge with phosphate groups and, deprotonated phosphate groups contribute to a decrease in the ζ-potential due to the negatively charged O atoms, confirming the successful PEGylation. Notably, the LSPR remained consistent when compared to the samples in water (Figure S14b, Supporting Information).

Plasmonic NPs are widely known to exhibit photothermal properties. To investigate these properties in the NCs, the samples were exposed to irradiation with an irradiance of 10 W cm^{-2} using the irradiation setup described in experimental methods (Figure S17, Supporting Information). This irradiance level was chosen because it induces a temperature increase in water of less than 8 °C in the time span of 1 min (Figure S18, Supporting Information). The NCs were irradiated until reaching the boiling point (≈95 °C) at three different concentrations: 50, 25, and 10 pM (**Figure 4**a–c). The results demonstrated that the time required to reach the boiling point of water (Figure 4d) decreased when the thickness of the NCs shell decreased, as is schematically depicted in Figure 4f. Interestingly, the differences between AuB(10)@PCN-224@PEG and AuB(5)@PCN-224@PEG are less pronounced at a high concentration of 50 pM, while these differences become more significant as the concentration decreases. This can be attributed to the slight disparity in size between these two NCs, with AuB(10)@PCN-224@PEG and AuB(5)@PCN-224@PEG having sizes of 138 nm and 160 nm, respectively. In contrast, AuB(1)@PCN-224@PEG is nearly twice as large, measuring 276 nm (Table S2 and S5, Supporting Information). Differences in the heat generation of each of these NCs are clearly observed in Figure 4d which illustrates the time (s) required to reach water boiling temperature.

All the NCs at a concentration of 50 pM were exposed to heating cycles, wherein the same behavior of shell-thickness versus the rate of heating the medium was observed. This behavior was consistently replicated in at least four cycles (Figure 4e), with each cycle reaching the boiling point of water. Furthermore, the times required to reach the boiling point of water (23, 26, and 42 s for AuB@PCN-224@PEG (10), (5) and (1), respectively) were virtually identical, indicating that the PCN-224 shell prevents the reshaping and/or etching of the AuB@PCN-224@PEG when exposed to high temperatures conserving the characteristic LSPR band around 810 nm confirms that there is no alteration in the plasmonic properties (Figure S14c, Supporting Information). The confined space within the MOF shell effectively restricts these undesirable structural changes which were clearly observed with the uncoated AuB (Figure S19, Supporting Information).

Finally, cooling cycles were monitored and differences in the time to reach 30 °C were observed (Figure 4e), i.e., 5.92, 6.08, and 7.58 min for AuB(10)@PCN-224@PEG, AuB(5)@PCN-224@PEG, and AuB(1)@PCN-224@PEG, respectively. These differences are explained due to the heat transfer pathway through a thermal insulator material (Table S2, Supporting Information), such as a MOF, which requires more time to dissipate this heat into the surrounding medium.

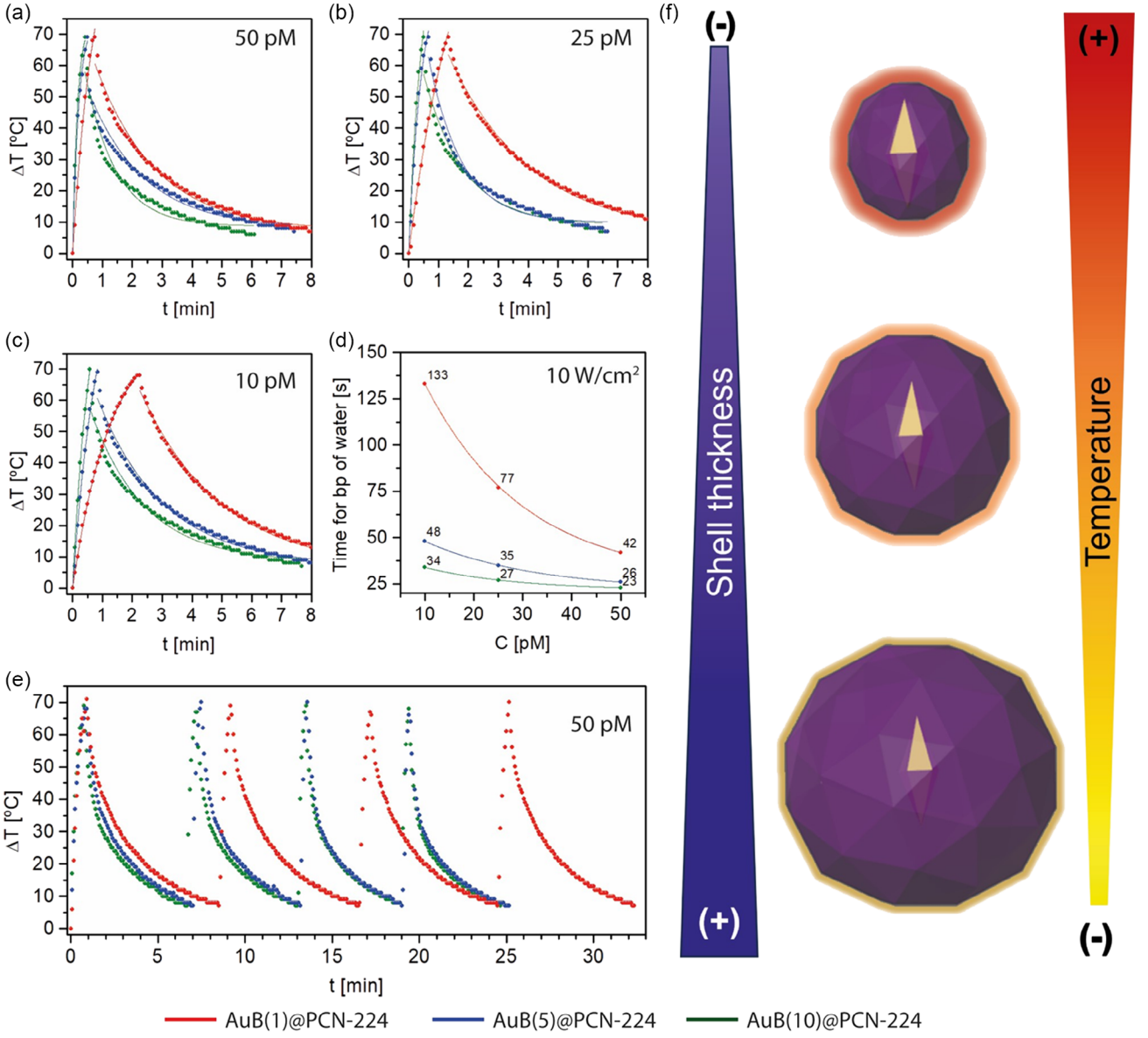

Figure 4. a–c) Heating curves of AuB@PCN-224@PEG NCs at different concentrations, d) graph of concentration dependence of the NCs to reach the boiling point of water, e) heating curve of the NCs applying 4 cycles, and f) graph of an inverse temperature dependence with the thickness of the MOF shell in the NCs.

2.4. Photostimulation of AuBipy@PCN-224@PEG inside Living Cells

Before the in vitro studies, the colloidal stability was studied for 120 h in different media (water, complete cell media (Dulbecco's modified eagle medium (DMEM)), and phosphate-buffered saline (PBS), Figure S20, Supporting Information). NCs remained colloidally stable in all cases, being this stability increased upon PEGylation. Then the interaction of the PEGylated NMOFs and NCs with cells was analyzed using 2D cell cultures of A549 adenocarcinoma cells. First, cell viability was analyzed by determining the cellular metabolic activity by an 3-(4,5-dimethylazol-2-yl)-2,5-diphenyltetrazolim bromide (MTT) assay. This study confirmed the high viability related to the NMOFs and the NCs using different concentrations. We used values of up to 0.5 nM (corresponding to ≈50 μg mL^{-1} of Zr), which showed no significant toxicity for any sample after 24 h of incubation (**Figure 5**a). These results are in good agreement with previous toxicity tests reported with the PCN family particles. Due to the low cytotoxicity of the Zr, this family of MOFs has a high biocompatibility, as Zr is one of the rare transition metals that are naturally present in the human body (≈300 mg of Zr).[19]

In vitro cellular uptake of the samples was also evaluated with flow cytometry using the fluorescence of the PCN-224 porphyrin linker. Particles were exposed to A549 cells at different concentrations for 24 h. Results show an increasing cell uptake with the

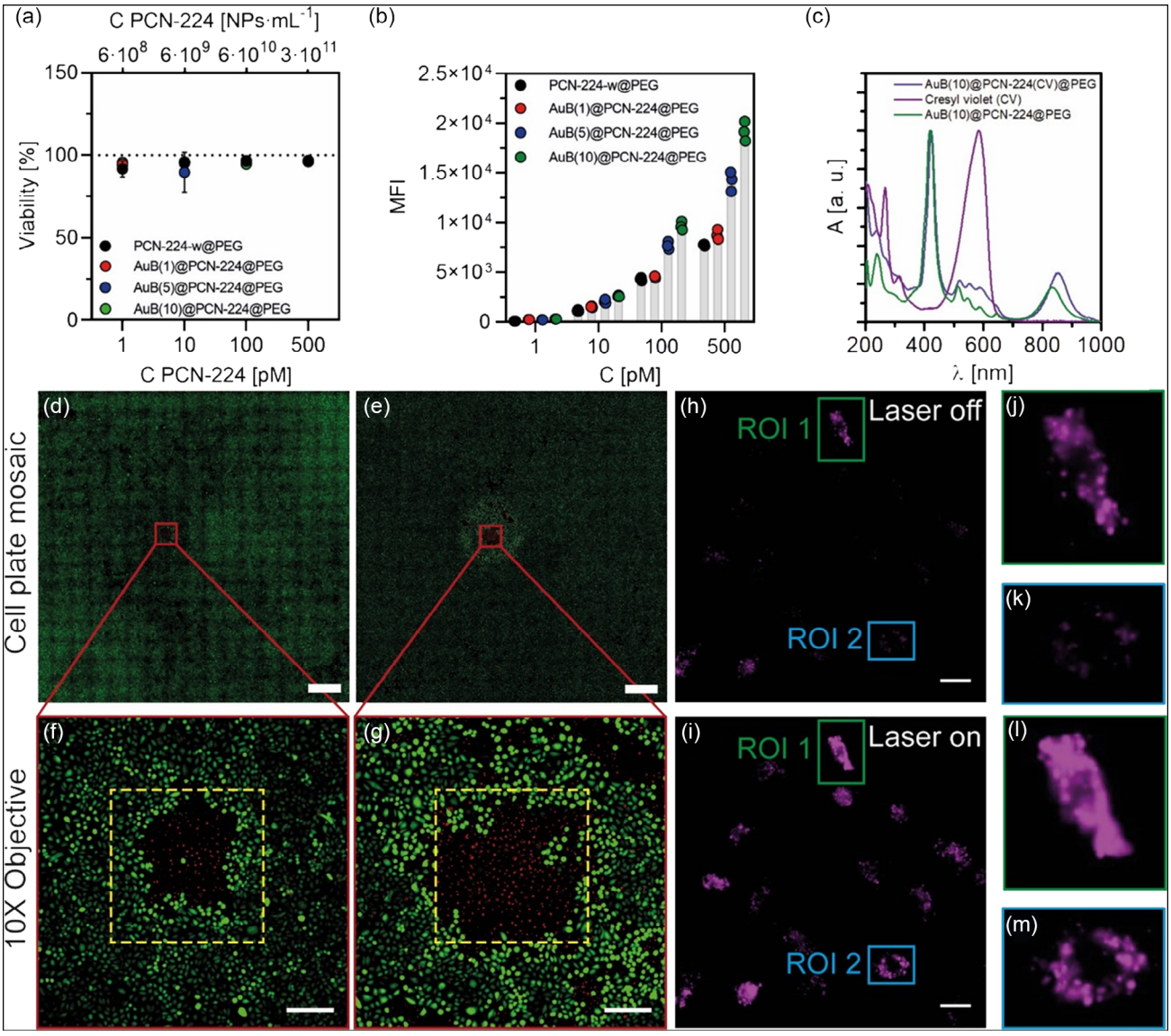

Figure 5. a) Cell viability values using MTT viability test, b) corrected cell uptake MFI values of PCN-224-w@PEG and AuB@PCN-224@PEG NCs after 24 h of incubation, and c) UV–vis spectra of AuB(10)@PCN-224@PEG loaded with CV. Cell plate mosaic reconstruction of an area of 1 cm^2 before irradiation d,e) in which a region of interest (inside the red square) after the irradiation with a 405 nm laser is highlighted f,g) (dashed yellow line represents the area irradiated with 405 nm laser) for (d,f) 2 min and (e,g) 5 min. h) Microscopy images before irradiation and i) after irradiation of selected areas. j,k) Specific ROIs before irradiation and l,m) ROIs before and after irradiation. Scale bars 1 mm for d,e, 200 µm for (f,g), and 20 µm for (h,i).

increment of the concentrations and a clear correlation of the mean fluorescence intensity (MFI) of the different samples related to the thickness of the shell in each case. This way, as the shell for the PCN-224-w@PEG and the AuB(1)@PCN-224@PEG is considerably larger than for the AuB(5)@PCN-224@PEG and AuB(10)@PCN-224@PEG, the MFI resulting from the same particle concentration leads to higher values for the first ones (Figure S21, Supporting Information). The obtained values were corrected using a correction factor calculated from the fluorescence measurements of each sample in the same conditions employed for the cytometer experiments (Table S6, Supporting Information). Thus, we can appreciate that the tendency changes and the internalization is inversely proportional to the thickness of the shell NCs´ size, indicating that smaller NCs are more efficiently internalized (Figure 5b).

Then, we studied the uptake of the AuB(10)@PCN-224@PEG using fluorescence microscopy as this NC was the one with the highest internalization rate. For this, we used CV-loaded NCs (Figure 5c). CV was selected as cargo for three reasons: 1) to prove the abilities of the NCs as drug nanocarriers; 2) to provide the NMOFs with an additional fluorescence signal; and 3) due to its ability to target functional lysosomes. Epifluorescence microscopy imaging experiments showed the intracellular location of the NMOF in the perinuclear region, as expected (Figure S22, Supporting Information). This intracellular localization indicates a clear colocalization of the CV and the NMOFs, confirming that

NCs are capable of storing intracellularly the CV. This ability is related to the PEG functionalization which prevents CV unspecific leaking.

Besides the good internalization and biocompatibility of the PCN-224@PEG NCs, these structures have other interesting characteristics for their use in biomedicine. This is due to two main features: 1) the MOF shell can be used for photodynamic therapy (PDT), as the porphyrin linkers of the structure are light-activable photosensitizers (PSs) that can create cytotoxic ROS and cause cell death[73] and 2) the NCs can serve as a good example of stimuli-responsive DDSs, as the AuB cores can get excited by NIR light irradiation generating temperature gradients that lead to the release of an encapsulated cargo in a controlled manner.[74] Here, we have explored the abilities of our NCs to explode both behaviors.

First, to study the in vitro induced cytotoxicity of the systems acting as PDT agents Figure 5d–g), A549 cells loaded with NCs were irradiated with a 405 nm laser (see Experimental Section). This excitation wavelength was specifically selected considering the high extinction coefficient of PCN-224 in the range of 400–450 nm, where the Soret band is located.

Two different irradiation times were tested, i.e., 2 and 5 min. Right after the sample irradiation, we performed a live-dead assay employing calcein-AM and propidium iodide as reporters for viable and dead cells, respectively. As shown in Figure 5d,e and their corresponding magnifications (Figure 5f,g), we can clearly see the induced cell death (PI tinction, in red) corresponding to the irradiated area, whereas the rest of the sample presents calcein tinction (green) indicating the viability of the nonirradiated NCs-loaded cells. Furthermore, when control cells without NCs were irradiated using equivalent conditions, the complete sample showed a calcein tinction for both irradiation conditions (Figure S23, Supporting Information). These results confirm the ability of our porphyrin-based NCs to act as efficient PDT agents when subjected to 405 nm laser irradiation. It is widely recognized that porphyrin molecules have the capacity to generate ROS, including singlet oxygen ($^1O_2$), when exposed to appropriate illumination.[75–77] Specifically, the triplet excited state of porphyrin, achieved through electron promotion from the ground state to the singlet excited state and subsequent intersystem crossing, can transfer its energy to adjacent molecular oxygen, resulting in the formation of $^1O_2$, which induces cell apoptosis.

In contrast, we studied the stimuli–responsive effectivity to release an encapsulated cargo by the excitation with a NIR laser (808 nm) coupled to the fluorescence microscope via a laser scanner, which allows the irradiation with a spatial and temporal control of selected areas (Figure 5h,i and S24, Supporting Information). Like to the previous experiments, A549 cells were incubated with CV-loaded AuB(10)@PCN-224@PEG NCs. As previously mentioned, particles showed accumulation (magenta-colored dots) in the lysosomes. As discussed above, and shown in Figure S20, Supporting Information, CV remained encapsulated into the NC´s pores even once they were internalized by the cells. After loading the cells with NCs, single cells were selected and irradiated using NIR light to evaluate the induced release of the encapsulated CV, which is evidenced before and after irradiation (Figure 5h,i, respectively). To illustrate this process, two regions of interest containing a single cell (ROI 1 and 2) are shown in magnified images (before and after irradiation in Figure 5j,k and l,m, respectively). These areas were immediately inspected after the irradiation, showing a clear increase in the fluorescence intensity of the CV channel. The CV-controlled release is associated with the local increment of the temperature in the surroundings of the AuB upon NIR irradiation, leading to a release of the CV encapsulated from the NC´s pores.

In conclusion, we have demonstrated the potential of our NCs as a promising strategy for therapeutics and diagnosis. This system offers a synergic effect between the porphyrin-based MOF for PDT and the thermoplasmonic response of the core of the system for triggered drug delivery.

3. Conclusion

We have introduced a facile seed-growth method to produce plasmonic core@shell NCs comprising a single AuB core and a PCN-224 shell. This approach enables precise control of the PCN-224 shell thickness by adjusting the AuB seed concentration while preserving the AuB morphology and properties. The NCs exhibit the photoluminescent features derived from the PCN-224 shell with an influence of the plasmonic core. In general, thinner shells correlate with more pronounced photoluminescent changes. Nevertheless, all the NCs were capable to generate ROS.

Heating dynamics of PEGylated NCs upon NIR light irradiation were analyzed, revealing a direct relationship between shell thickness and their heating/cooling behavior. Specifically, thicker shells result in slower heating and extended cooling.

The good biocompatibility of PEGylated NCs was proven in in vitro studies. NCs were readily internalized by cells in a size-manner fashion, i.e., the smaller the NCs (AuB(10)@PCN-224@PEG), the greater the internalization rates. Two applications were explored in vitro. First, they were used as PDT agents. They effectively killed cancer cells exposed to a 405 nm laser, leaving untreated cells unharmed. Second, PEGylated NCs loaded with CV showcased an efficient NIR-induced release of CV through a thermodiffusion mechanism. In conclusion, our NCs stand out as potent tools for integrative therapeutic and imaging applications.

4. Experimental Section

AuB synthesis,[47] PEGylation[78] and phase transfer of AuB,[79] synthesis of PCN-224 NPs,[80] and PEGylation of AuB@PCN-224 to give colloidal stability with mPEG-PO_3[63] were adapted and scaled-up from previous reports. More detailed experimental protocols and characterization techniques are provided in the supporting information. Milli-Q water with a resistivity of 18.2 MΩ cm at 25 °C was used in all the experiments and for rinsing glass materials. All the reagents were used without any further modification.

Materials: All the reagents including phosphorus oxychloride ($POCl_3$, 99%, Sigma-Aldrich); poly(ethylene glycol) methyl ether (mPEG, Mn 5000, Sigma-Aldrich); triethylamine (≥99.5%, Sigma-Aldrich); dichloromethane (DCM, ≥99.8%, Fisher Scientific);hydrogen tetrachloroaurate (III) hydrate ($HAuCl_4$, Au≥49%, Thermo Scientific); hydrochloric acid (HCl, 37%); N,N-dimethylformamide (DMF, ≥99.8%, Fisher Scientific); chloroform ($CHCl_3$, ≥99.8%, Fisher Scientific); silver nitrate ($AgNO_3$, ≥99.0%, Sigma-Aldrich); L-Ascorbic acid ($C_6H_8O_6$, ≥99%, Sigma-Aldrich); sodium borohydride ($NaBH_4$, ≥98.0%, Sigma-Aldrich); citric acid (≥ 99.5%, Sigma-Aldrich); cetyltrimethylammonium chloride (CTAC, 25 wt% in H_2O, Sigma-Aldrich); hexadecyltrimethylammonium bromide (CTAB, ≥98%,

Sigma-Aldrich); poly(ethylene glycol) methyl ether thiol (MeO-PEG-SH, 2 kDa, Sigma Aldrich);zirconium (IV) n-butoxide (80 wt% in 1-butanol, Sigma-Aldrich); 5,10,15,20-(tetra-4-carboxyphenyl)porphyrin (TCPP, 98%, PorphyChem); 1-propanol (99.7%, Sigma-Aldrich); acetic acid glacial (CH_3COOH, 99.7%, Fisher Scientific); N,N-dimethylformamide (DMF, ≥99.8%, Fisher Scientific); benzoic acid (≥99.5%, Sigma-Aldrich); and methanol (MeOH) were used as purchased without any purification.

Synthesis of mPEG-PO_3: mPEG-PO_3 was synthesized using a slightly modified version of a previously reported method.[63] The synthesis was conducted in a two-neck flask, where 50 mmol of $POCl_3$ dissolved in 5 mL of DCM were initially added. Subsequently, 150 mmol of triethylamine was introduced at 0 °C. After 30 min, 15 mmol of mPEG 5 kDa was added to the mixture in 50 mL of DCM. The resulting solution was stirred at RT for a period of 10 h. Following the stirring process, 20 mL of water was added to the reaction mixture and allowed to react for an additional 3 h. Subsequently, the DCM solvent was removed under vacuum using a rotavapor, and the crude product was subjected to purification by dialysis, utilizing a dialysis membrane with a molecular weight cutoff of 3500. Finally, the residual water was eliminated through lyophilization, resulting in the formation of mPEG-PO_3 as a white solid.

Synthesis of Au Bipyramids (AuB): Synthesis of Pentatwinned Seeds: In a glass vial of 20 mL, initial seeds were prepared adding 8.639 mL of water together with 0.661 mL of the CTAC solution and 0.100 mL of $HAuCl_4$ 25 mM (in water) under vigorous magnetic stirring (1000 rpm) for 5 min. After that, 0.1 mL of citric acid 0.5 M (in water) was added to the mixture of reaction, and immediately two doses nonstop of 0.25 mL of freshly prepared $NaBH_4$ 25 mM (in water). The solution turned from pale yellow to brownish solution indicating the formation of gold seeds. After 2 min of stirring, the vial was closed, and these seeds were heated in a heating block at 80 °C for 90 min under gentle stirring (300 rpm). Finally, the color of the solution changed from brown to red indicating that the aging process was successful in creating the pentatwinned defects. The solution was stored at RT.

Scaled-Up AuB Synthesis: In a glass bottle of 1 L, the growth solution of AuB was prepared by adding under magnetic stirring (500 rpm) 275 mL of water, 250 mL of CTAB 0.2 M, 10 mL of $HAuCl_4$ 25 mM, 5 mL of $AgNO_3$ 10 mM, 0.833 mL of HCl, and 4 mL of ascorbic acid 0.1 M (all in water). After the change of color from orange-yellow to colorless with the addition of the ascorbic acid, 12 mL of pentatwinned seeds were added. The mixture of reaction was kept at 30 °C for 2 h. After this, the NPs were washed with water three times to remove CTAB excess and left in a final volume of 10 mL of water.

PEGylation and Phase Transfer of AuB: AuB without the CTAB excess presents a LSPR around 808 nm. At this wavelength, the absorption molar coefficient is $3.63 \times 10^{10}\ M^{-1}\ cm^{-1}$. The number of chains of MeO-PEG-SH used for the PEGylation was 500 000 chains per particle. A 1% of this total amount (5000 chains) was added to the colloidal dispersion of AuB, which means that 75 µL of MeO-PEG-SH and 20 mg mL^{-1} solution were added to 10 mL of 15 nM AuB in water. In a separate tube, 150 mg of MeO-PEG-SH, which would correspond to 500 000 chains per particle, were dissolved in chloroform. The NPs in water and the PEG solution in chloroform were mixed in a separation funnel and strongly shaken followed by the addition of 10 mL of methanol for beginning the phase transfer from aqueous to organic phase. The emulsion formed was destroyed with the addition of more water. Once the AuB was in the organic phase, they were collected and dried under rotatory evaporation and redispersed in the same volume of DMF as they were in the beginning.

Synthesis of PCN-224: Preparation of Zr6 Cluster: 100 mL of 1-propanol and 5 mL of Zr (IV) n-butoxide (80 wt%) were mixed and stirred for 10 min. Then, 33 g of benzoic acid was added, and the mixture was ultrasonicated for 20 more minutes. After that, it was heated at reflux and stirred overnight. The next day, it was rotavapored and the solid product was washed 3 times with 1-propanol and 10 min of centrifugation at 7000 rcf. The final product was dried under a vacuum at RT. This cluster was used for the synthesis of PCN-224-p and AuB@PCN-224. For PCN-224-w, the nonvolatile remnants of 1-propanol were washed and removed with MeOH, and the solid was dried under vacuum at RT.

MOF Synthesis: 20 mg of Zr_6-oxo cluster was added together with 0.8 mL of acetic acid and 0.2 mL of DMF in a glass vial. In an Eppendorf tube, 10 mg of TCPP linker were weighed and dissolved in 1 mL of DMF or in 1 mL of AuB DMF solution using ultrasonication. The mixture in the vial was stirred with a magnetic bar at 300 rpm and then the solution of the Eppendorf tube was added. The reaction was carried out at RT for 1 h. The resulting solution was sonicated and collected in a 2 mL Eppendorf tube and centrifugated at 10 000 rcf for 10 min. It was washed 3 times with 1 mL of DMF and 3 more with 1 mL of MeOH and centrifugated each of them (10 min, 10 000 rcf). It was left in 1 mL of MeOH.

Cresyl Violet Loading: PCN-224 or AuB@PCN-224 NCs, 200 µL dispersions at a concentration of 1 mg mL^{-1} of solid in methanol (MeOH) were combined with a solution of CV in water (200 µL, 2 mg mL^{-1}). The resulting mixture was incubated overnight at RT under continuous shaking. After incubation, the NMOFs or NCs were separated from the solution by centrifugation at 10 000 rpm for 10 min.

PCN-224 PEGylation: The surface modification of PCN-224 was carried out using the mPEG-PO_3 polymer. To accomplish this, the product of one synthesis of PCN-224-w or AuB@PCN-224 in water was combined with 2.5 mL of a 25 mg mL^{-1} aqueous solution of mPEG-PO_3. The resulting mixture was stirred using a magnetic bar at a speed of 500 rpm for 3 h. Subsequently, the coated material underwent a washing procedure consisting of three water washes. Each wash involved centrifugation at 10 000 rcf for a duration of 10 min.

Cell Culture: The A549 cell line, derived from human lung carcinoma, was maintained in a culture of DMEM with phenol red, containing 4.5 g L^{-1} of D-glucose, L-glutamine, and pyruvate. This culture medium (DMEM Gibco, Thermo Fisher Scientific, Massachusetts, USA) was further supplemented with 10% fetal bovine serum (Gibco, Thermo Fisher, Massachusetts, USA) and 1% penicillin/streptomycin (P/S, Gibco, Thermo Fisher Scientific, Massachusetts, USA) to create complete DMEM (cDMEM). Cell culture was conducted at a constant temperature of 37 °C, within a 5% CO_2 atmosphere, and maintained under humid conditions. Subsequently, when the cells reached 80% confluency, they were subjected to a washing step using Dulbecco's PBS (Thermo Fisher #14 190 169) before being passaged. The passaging process involved incubating the cells with 0.25% trypsin-ethylenediaminetetraacetic acid (Gibco, Thermo Fisher Scientific, Massachusetts, USA) to facilitate detachment and subsequent subculture.

Laser Irradiation (Heating Experiments): For the laser irradiation experiments, the samples were placed in the wells of a 96-well plate. Depending on the specific experiment described in each section, the samples either contained cells or did not. Irradiation was performed using an 808 nm laser (Lasing, #FC-W-808A) coupled to a zoom fiber collimator (Thorlabs, #ZC618SMA-B). This collimator was utilized to control the spot size and ensure homogeneous irradiation of the cells.

To determine the intensity of the laser irradiation received by the cells, a power energy meter (Thorlabs, #PM100D) equipped with a thermal power head (10 W, 25 mm, Thorlabs, #S425C) was employed to measure the output power. The spot size was determined by using a viewing card (Thorlabs, #VRC4) to visualize the spot, and ImageJ software was utilized to measure its dimensions. Since the beam was collimated, a uniform spot distribution was assumed, allowing the intensity to be calculated by dividing the power (7.85 W) by the surface area (0.785 cm^2) of the spot giving an irradiance of 10 W cm^{-2}. Various experimental conditions involving different time intervals and power densities were investigated, as specified in each individual experiment.

Microscopy Imaging: A549 cells were initially seeded onto µ-slide 8 well-ibiTreat chambers, with each well having a surface area of 1 cm^2 (Ibidi, Germany, #80 826). The seeding density used was 20 000 cells per well, and they were cultured in cDMEM for 24 h.

After the 24 h incubation period, the cDMEM was replaced with freshly prepared solutions of PCN-224 and AuB@PCN-224 with and without CV at a concentration of 100 pM, diluted in cDMEM. Following a 3 h exposure to these particles, the cells underwent a single rinse with 1X PBS. This step aimed to eliminate any noninternalized particles that might have remained dispersed in the cDMEM prior to the subsequent image acquisition.

Fluorescence images of the cells were captured using a Leica Microscope type DMI8, equipped with a Leica DFC9000 camera, and

maintained in an incubator at a temperature of 37 °C under a 5% CO_2 atmosphere. To analyze the images, ImageJ software was utilized for image processing and data extraction.

NIR irradiation of the samples was performed using Leica infinity scanner installed in the microscope that allows the scanning of the selected ROIs with a NIR laser using LAS X software.

To study the PDT effect of the particles, AuB@PCN-224 was excited with a 405 nm laser in a confocal microscope. The experiments were performed using an Andor Dragonfly spinning disk confocal system mounted on a Nikon TiE microscope equipped with a Zyla 4.2 PLUS camera (Andor, Oxford Instruments) and an OKO-lab incubator to keep cells at 37 °C under a 5% CO_2 atmosphere during the whole experiment. Samples were irradiated for 2 and 5 min. To study the viability, a live-dead assay employing calcein-AM and propidium iodide was employed as reporters for viable and apoptotic cells, respectively. All the images were processed with ImageJ.

Supporting Information

Supporting Information is available from the Wiley Online Library or from the author.

Acknowledgements

The authors acknowledge the financial support of the MCIN/AEI (PID2020-119206RB-I00, PID2019-108624RB-I00, RYC-2019-028238-I), the Xunta de Galicia (ED431F 2017/02, ED431F 2020/11, 2021-CP090, Centro Singular de Investigación de Galicia Accreditation 2019–2022, ED431G 2019/03), the European Union (European Regional Development Fund – ERDF; H2020-MSCA-ITN grant agreement no. 860942; H2020-FET-Open grant agreement no. 899612; and H2020-ICT grant agreement no. 10101694), and the European Research Council (starting grant no. 950421). M.C. acknowledges to H2020-MSCA-ITN grant agreement no. 860942. M.C.-M. thanks the AEI (FPU19/03155). J.M.V.-F. acknowledges the Spanish Ministry of Science and Innovation for his postdoctoral grant (IJC2020-044369-I). The authors are grateful for the use of RIAIDT-USC analytical facilities.

Conflict of Interest

The authors declare no conflict of interest.

Author Contributions

M.C. and S.F.-H carried out the synthesis and characterization of the materials. G.Z., M.C.-M., and J.M.V.-F. performed the photoluminescence characterization, cell studies, and the TEM and EDX characterization, respectively. The manuscript was written through the contributions of all authors. All authors have approved the final version of the manuscript.

Data Availability Statement

The data that support the findings of this study are available from the corresponding author upon reasonable request.

Keywords

drug delivery, photodynamic therapy, porous coordination network, thermoplasmonics, Zr(IV)-based porphyrinic metal−organic frameworks

Received: November 7, 2023
Revised: February 1, 2024
Published online:

[1] S. Seth, A. J. Matzger, *Cryst. Growth Des.* **2017**, *17*, 4043.
[2] M. Eddaoudi, D. B. Moler, H. Li, B. Chen, T. M. Reineke, M. O'Keeffe, O. M. Yaghi, *Acc. Chem. Res.* **2001**, *34*, 319.
[3] M. J. Kalmutzki, N. Hanikel, O. M. Yaghi, *Sci. Adv.* **2018**, *4*, eaat9180.
[4] J. H. Cavka, S. Jakobsen, U. Olsbye, N. Guillou, C. Lamberti, S. Bordiga, K. P. Lillerud, *J. Am. Chem. Soc.* **2008**, *130*, 13850.
[5] K. J. Gagnon, H. P. Perry, A. Clearfield, *Chem. Rev.* **2012**, *112*, 1034.
[6] R. Banerjee, A. Phan, B. Wang, C. Knobler, H. Furukawa, M. O'Keeffe, O. M. Yaghi, *Science* **2008**, *319*, 939.
[7] N. M. Padial, J. Castells-Gil, N. Almora-Barrios, M. Romero-Angel, I. Da Silva, M. Barawi, A. García-Sánchez, V. A. De La Peña O'Shea, C. Martí-Gastaldo, *J. Am. Chem. Soc.* **2019**, *141*, 13124.
[8] I. M. Hönicke, I. Senkovska, V. Bon, I. A. Baburin, N. Bönisch, S. Raschke, J. D. Evans, S. Kaskel, *Angew. Chem., Int. Ed.* **2018**, *57*, 13780.
[9] O. K. Farha, I. Eryazici, N. C. Jeong, B. G. Hauser, C. E. Wilmer, A. A. Sarjeant, R. Q. Snurr, S. T. Nguyen, A. Ö. Yazaydin, J. T. Hupp, *J. Am. Chem. Soc.* **2012**, *134*, 15016.
[10] H. Furukawa, N. Ko, Y. B. Go, N. Aratani, S. B. Choi, E. Choi, A. Ö. Yazaydin, R. Q. Snurr, M. O'Keeffe, J. Kim, O. M. Yaghi, *Science* **2010**, *329*, 424.
[11] J. R. Holst, A. I. Cooper, *Adv. Mater.* **2010**, *22*, 5212.
[12] X. Yin, A. Alsuwaidi, X. Zhang, *Microporous Mesoporous Mater.* **2022**, *330*, 111633.
[13] M. Kalaj, S. M. Cohen, *ACS Cent. Sci.* **2020**, *6*, 1046.
[14] G. E. Decker, Z. Stillman, L. Attia, C. A. Fromen, E. D. Bloch, *Chem. Mater.* **2019**, *31*, 4831.
[15] S. Dai, C. Simms, I. Dovgaliuk, G. Patriarche, A. Tissot, T. N. Parac-Vogt, C. Serre, *Chem. Mater.* **2021**, *33*, 7057.
[16] Z. Chen, J. Li, T. Li, T. Fan, C. Meng, C. Li, J. Kang, L. Chai, Y. Hao, Y. Tang, O. A. Al-Hartomy, S. Wageh, A. G. Al-Sehemi, Z. Luo, J. Yu, Y. Shao, D. Li, S. Feng, W. J. Liu, Y. He, X. Ma, Z. Xie, H. Zhang, *Natl. Sci. Rev.* **2022**, *9*, nwac104.
[17] F. Zheng, Z. Chen, J. Li, R. Wu, B. Zhang, G. Nie, Z. Xie, H. Zhang, *Adv. Sci.* **2022**, *9*, 2105231.
[18] Z. Chen, C. Wu, Y. Yuan, Z. Xie, T. Li, H. Huang, S. Li, J. Deng, H. Lin, Z. Shi, C. Li, Y. Hao, Y. Tang, Y. You, O. A. Al-Hartomy, S. Wageh, A. G. Al-Sehemi, R. Lu, L. Zhang, X. Lin, Y. He, G. Zhao, D. Li, H. Zhang, *J. Nanobiotechnol.* **2023**, *21*, 141.
[19] M. Ceballos, M. Cedrún-Morales, M. Rodríguez-Pérez, S. Funes-Hernando, J. M. Vila-Fungueiriño, G. Zampini, M. F. Navarro Poupard, E. Polo, P. del Pino, B. Pelaz, *Nanoscale* **2022**, *14*, 6789.
[20] S. Mallakpour, E. Nikkhoo, C. M. Hussain, *Coord. Chem. Rev.* **2022**, *451*, 214262.
[21] D. G. Madden, D. O'Nolan, N. Rampal, R. Babu, C. Çamur, A. N. Al Shakhs, S. Y. Zhang, G. A. Rance, J. Perez, N. Pietro Maria Casati, C. Cuadrado-Collados, D. O'Sullivan, N. P. Rice, T. Gennett, P. Parilla, S. Shulda, K. E. Hurst, V. Stavila, M. D. Allendorf, J. Silvestre-Albero, A. C. Forse, N. R. Champness, K. W. Chapman, D. Fairen-Jimenez, *J. Am. Chem. Soc.* **2022**, *144*, 13729.
[22] R. Zhao, Z. Liang, R. Zou, Q. Xu, *Joule* **2018**, *2*, 2235.
[23] Z. Zheng, H. L. Nguyen, N. Hanikel, K. K. Y. Li, Z. Zhou, T. Ma, O. M. Yaghi, *Nat. Protoc.* **2023**, *18*, 136.
[24] R. M. Rego, G. Kuriya, M. D. Kurkuri, M. Kigga, *J. Hazard. Mater.* **2021**, *403*, 123605.
[25] Y. Shi, A. F. Yang, C. S. Cao, B. Zhao, *Coord. Chem. Rev.* **2019**, *390*, 50.
[26] D. K. Sannes, S. Øien-ØDegaard, E. Aunan, A. Nova, U. Olsbye, *Chem. Mater.* **2023**, *35*, 3793.

[27] C. Koschnick, R. Stäglich, T. Scholz, M. W. Terban, A. von Mankowski, G. Savasci, F. Binder, A. Schökel, M. Etter, J. Nuss, R. Siegel, L. S. Germann, C. Ochsenfeld, R. E. Dinnebier, J. Senker, B. V. Lotsch, *Nat. Commun.* **2021**, *12*, 3099.
[28] W. Morris, B. Volosskiy, S. Demir, F. Gándara, P. L. McGrier, H. Furukawa, D. Cascio, J. F. Stoddart, O. M. Yaghi, *Inorg. Chem.* **2012**, *51*, 6443.
[29] D. Feng, Z. Y. Gu, Y. P. Chen, J. Park, Z. Wei, Y. Sun, M. Bosch, S. Yuan, H. C. Zhou, *J. Am. Chem. Soc.* **2014**, *136*, 17714.
[30] D. Feng, Z.-Y. Gu, J.-R. Li, H.-L. Jiang, Z. Wei, H.-C. Zhou, *Angew. Chem.* **2012**, *124*, 10453.
[31] H. L. Jiang, D. Feng, K. Wang, Z. Y. Gu, Z. Wei, Y. P. Chen, H. C. Zhou, *J. Am. Chem. Soc.* **2013**, *135*, 13934.
[32] P. Deria, D. A. Gómez-Gualdrón, I. Hod, R. Q. Snurr, J. T. Hupp, O. K. Farha, *J. Am. Chem. Soc.* **2016**, *138*, 14449.
[33] D. Feng, W. C. Chung, Z. Wei, Z. Y. Gu, H. L. Jiang, Y. P. Chen, D. J. Darensbourg, H. C. Zhou, *J. Am. Chem. Soc.* **2013**, *135*, 17105.
[34] X. Guo, N. Zhu, Y. Lou, S. Ren, S. Pang, Y. He, X. B. Chen, Z. Shi, S. Feng, *Chem. Commun.* **2020**, *56*, 5389.
[35] X. Sun, Q. Wang, H. Bao, Y. Liu, S. Yao, M. Li, N. Chen, Y. Chen, *ACS Appl. Nano Mater.* **2024**, https://doi.org/10.1021/acsanm.3c04675.
[36] S. C. Qi, Z. H. Yang, R. R. Zhu, X. J. Lu, D. M. Xue, X. Q. Liu, L. B. Sun, *J. Mater. Chem. A* **2021**, *9*, 24510.
[37] S. Yuan, L. Feng, K. Wang, J. Pang, M. Bosch, C. Lollar, Y. Sun, J. Qin, X. Yang, P. Zhang, Q. Wang, L. Zou, Y. Zhang, L. Zhang, Y. Fang, J. Li, H. C. Zhou, *Adv. Mater.* **2018**, *30*, 1704303.
[38] X. Zhang, M. C. Wasson, M. Shayan, E. K. Berdichevsky, J. Ricardo-Noordberg, Z. Singh, E. K. Papazyan, A. J. Castro, P. Marino, Z. Ajoyan, Z. Chen, T. Islamoglu, A. J. Howarth, Y. Liu, M. B. Majewski, M. J. Katz, J. E. Mondloch, O. K. Farha, *Coord. Chem. Rev.* **2021**, *429*, 213615.
[39] R. Yu, L. M. Liz-Marzán, F. J. García De Abajo, *Chem. Soc. Rev.* **2017**, *46*, 6710.
[40] W. Simons, D. Gonnissen, A. Hubin, *J. Electroanal. Chem.* **1997**, *433*, 141.
[41] L. Wang, M. Hasanzadeh Kafshgari, M. Meunier, *Adv. Funct. Mater.* **2020**, *30*, 2005400.
[42] G. Mie, *Ann. Phys.* **1908**, *25*, 377.
[43] J. Pérez-Juste, I. Pastoriza-Santos, L. M. Liz-Marzán, P. Mulvaney, *Coord. Chem. Rev.* **2005**, *249*, 1870.
[44] L. Scarabelli, M. Coronado-Puchau, J. J. Giner-Casares, J. Langer, L. M. Liz-Marzán, *ACS Nano* **2014**, *8*, 5833.
[45] J. E. Park, Y. Lee, J. M. Nam, *Nano Lett.* **2018**, *18*, 6475.
[46] I. B. Becerril-Castro, I. Calderon, N. Pazos-Perez, L. Guerrini, F. Schulz, N. Feliu, I. Chakraborty, V. Giannini, W. J. Parak, R. A. Alvarez-Puebla, *Anal. Sens.* **2022**, *2*, e202200005.
[47] A. Sánchez-Iglesias, N. Winckelmans, T. Altantzis, S. Bals, M. Grzelczak, L. M. Liz-Marzán, *J. Am. Chem. Soc.* **2017**, *139*, 107.
[48] J. Langer, D. J. de Aberasturi, J. Aizpurua, R. A. Alvarez-Puebla, B. Auguié, J. J. Baumberg, G. C. Bazan, S. E. J. Bell, A. Boisen, A. G. Brolo, J. Choo, D. Cialla-May, V. Deckert, L. Fabris, K. Faulds, F. Javier García de Abajo, R. Goodacre, D. Graham, A. J. Haes, C. L. Haynes, C. Huck, T. Itoh, M. Käll, J. Kneipp, N. A. Kotov, H. Kuang, E. C. Le Ru, H. K. Lee, J. F. Li, X. Y. Ling, et al. *ACS Nano* **2020**, *14*, 28.
[49] A. Balestri, J. Cardellini, D. Berti, *Curr. Opin. Colloid Interface Sci.* **2023**, *66*, 101710.
[50] M. Kim, J. H. Lee, J. M. Nam, *Adv. Sci.* **2019**, *6*, 1900471.
[51] E. Polo, M. F. Navarro Poupard, L. Guerrini, P. Taboada, B. Pelaz, R. A. Alvarez-Puebla, P. del Pino, *Nano Today* **2018**, *20*, 58.
[52] C. Carrillo-Carrión, R. Martínez, M. F. Navarro Poupard, B. Pelaz, E. Polo, A. Arenas-Vivo, A. Olgiati, P. Taboada, M. G. Soliman, Ú. Catalán, S. Fernández-Castillejo, R. Solà, W. J. Parak, P. Horcajada, R. A. Alvarez-Puebla, P. del Pino, *Angew. Chem., Int. Ed.* **2019**, *58*, 7078.
[53] C. Carrillo-Carrión, R. Martínez, E. Polo, M. Tomás-Gamasa, P. Destito, M. Ceballos, B. Pelaz, F. López, J. L. Mascareñas, P. Del Pino, *ACS Nano* **2021**, *15*, 16924.
[54] K. Kantner, J. Rejman, K. V. L. Kraft, M. G. Soliman, M. V. Zyuzin, A. Escudero, P. del Pino, W. J. Parak, *Chem. - A Eur. J.* **2018**, *24*, 2098.
[55] M. Pérez-Hernández, P. Del Pino, S. G. Mitchell, M. Moros, G. Stepien, B. Pelaz, W. J. Parak, E. M. Gálvez, J. Pardo, J. M. De La Fuente, *ACS Nano* **2015**, *9*, 52.
[56] C. Bao, N. Beziere, P. Del Pino, B. Pelaz, G. Estrada, F. Tian, V. Ntziachristos, J. M. De La Fuente, D. Cui, *Small* **2013**, *9*, 68.
[57] E. Polo, P. Del Pino, B. Pelaz, V. Grazu, J. M. De la Fuente, *Chem. Commun.* **2013**, *49*, 3676.
[58] J. W. M. Osterrieth, D. Fairen-Jimenez, *Biotechnol. J.* **2021**, *16*, 2000005.
[59] M. A. Rahman, M. Z. Saghir, *Int. J. Heat Mass Transf.* **2014**, *73*, 693.
[60] R. Martínez, C. Carrillo-Carrión, P. Destito, A. Alvarez, M. Tomás-Gamasa, B. Pelaz, F. Lopez, J. L. Mascareñas, P. del Pino, *Cell Rep. Phys. Sci.* **2020**, *1*, 100076.
[61] Y. Li, W. S. Lo, F. Zhang, X. Si, L. Y. Chou, X. Y. Liu, B. P. Williams, Y. H. Li, S. H. Jung, Y. S. Hsu, F. S. Liao, F. K. Shieh, M. N. Ismail, W. Huang, C. K. Tsung, *J. Am. Chem. Soc.* **2021**, *143*, 5182.
[62] C. Mottillo, T. Friščić, *Angew. Chem.* **2014**, *126*, 7601.
[63] X. Chen, Y. Zhuang, N. Rampal, R. Hewitt, G. Divitini, C. A. O'Keefe, X. Liu, D. J. Whitaker, J. W. Wills, R. Jugdaohsingh, J. J. Powell, H. Yu, C. P. Grey, O. A. Scherman, D. Fairen-Jimenez, *J. Am. Chem. Soc.* **2021**, *143*, 13557.
[64] J. W. M. Osterrieth, D. Wright, H. Noh, C. W. Kung, D. Vulpe, A. Li, J. E. Park, R. P. Van Duyne, P. Z. Moghadam, J. J. Baumberg, O. K. Farha, D. Fairen-Jimenez, *J. Am. Chem. Soc.* **2019**, *141*, 3893.
[65] C. Chen, N. Hildebrandt, *TrAC, Trends Anal. Chem.* **2020**, *123*, 115748.
[66] C. S. Yun, A. Javier, T. Jennings, M. Fisher, S. Hira, S. Peterson, B. Hopkins, N. O. Reich, G. F. Strouse, *J. Am. Chem. Soc.* **2005**, *127*, 3115.
[67] N. Nwahara, O. J. Achadu, T. Nyokong, *J. Photochem. Photobiol., A* **2018**, *359*, 131.
[68] X. Cao, B. Hu, R. Ding, P. Zhang, *Phys. Chem. Chem. Phys.* **2015**, *17*, 14479.
[69] G. Zampini, L. Tarpani, G. Massaro, M. Gambucci, A. Nicoziani, L. Latterini, *ChemPhotoChem* **2017**, *1*, 553.
[70] L. Shi, L. Yang, H. Zhang, K. Chang, G. Zhao, T. Kako, J. Ye, *Appl. Catal., B* **2018**, *224*, 60.
[71] T. Burger, C. Winkler, I. Dalfen, C. Slugovc, S. M. Borisov, *J. Mater. Chem. C* **2021**, *9*, 17099.
[72] M. Peng, G. Guan, H. Deng, B. Han, C. Tian, J. Zhuang, Y. Xu, W. Liu, Z. Lin, *Environ. Sci. Nano* **2019**, *6*, 207.
[73] F. Yang, W. Yu, Q. Yu, X. Liu, C. Liu, C. Lu, X. Liao, Y. Liu, N. Peng, *Small* **2023**, *19*, 2206124.
[74] M. Cedrún-Morales, M. Ceballos, E. Polo, P. del Pino, B. Pelaz, *Chem. Commun.* **2023**, *59*, 2869.
[75] A. Schlachter, P. Asselin, P. D. Harvey, *ACS Appl. Mater. Interfaces* **2021**, *13*, 26651.
[76] J. Demel, P. Kubát, F. Millange, J. Marrot, I. Císařová, K. Lang, *Inorg. Chem.* **2013**, *52*, 2779.
[77] K. C. Park, C. Seo, G. Gupta, J. Kim, C. Y. Lee, *ACS Appl. Mater. Interfaces* **2017**, *9*, 38670.
[78] J. Hühn, C. Carrillo-Carrion, M. G. Soliman, C. Pfeiffer, D. Valdeperez, A. Masood, I. Chakraborty, L. Zhu, M. Gallego, Z. Yue, M. Carril, N. Feliu, A. Escudero, A. M. Alkilany, B. Pelaz, P. Del Pino, W. J. Parak, *Chem. Mater.* **2017**, *29*, 399.
[79] M. G. Soliman, B. Pelaz, W. J. Parak, P. del Pino, *Chem. Mater.* **2015**, *27*, 990.
[80] H. He, L. Li, Y. Liu, M. Kassymova, D. Li, L. Zhang, H. L. Jiang, *Nano Res.* **2021**, *14*, 444.